Supplementary Information

Supplementary Text 1

The GFED5-based reconstruction data version

As sensitivity test of methods in this study, besides the FireCCI51-based reconstruction, we also used burned area from GFED5 to reconstruct global monthly burned area maps with half-degree spatial resolution from 1901 to 2020. The procedures are the same as methods using FireCCI51 mentioned in the main text.

In the model validation based on the leave-one-year-out method, the multi-year (2003-2020) mean burned area fraction (BAF) between observation (GFED5) and our prediction is spatially consistent in general (Fig. S17). There is a strong spatial correlation between observations and prediction at the global scale with R^2 of 0.99 and a linear slope of 0.97 (Fig. S17a). Among all regions, R^2 ranges from 0.80 to 0.99, and slopes range from 0.81 to 0.97 (Fig. S17c-q), which indicates that the trained models can well reproduce the spatial patterns of burned area.

Additionally, our models reproduced the inter-annual variability of GFED5 well (Fig. S18). R^2 from the temporal regressions of global total burned area between predictions and observations is 0.91, and it ranges from 0.49 to 0.95 across regions. The linear slope is 0.79 for the global total burned area, and its range is 0.59-0.96 across regions. The model can also well capture the seasonality of burned area in each region (Fig. S19).

Supplementary Text 2

The FireCCI51-GDP data version

We calibrated the reconstructed burned area before 2000 at the regional scale using GDP as a proxy of anthropogenic effects (e.g., fire suppression, landscape fragmentation). The workflow of the calibration processes is illustrated in Fig. S23. We first calculated the annual regional GDP based on the annual national GDP from the Maddison Project Database 2023 (Bolt and Van Zanden, 2024) in all countries in a given region. We then derived annual regional total burned area (BA) from Mouillot and Field (2005). Among the 14 GFED regions, significant (p-value<0.05) linear correlations were found between the regional decade-averaged GDP and burned area (the BA-GDP linear correlation) in TENA, CEAM, NHSA, SHSA, NHAF, SEAS, EQAS and AUST (Fig. S24). We only selected these regions with a significant BA-GDP correlation to calibrate the original FireCCI51-based burned area using GDP, and burned area in regions without a significant correlation remained unchanged. Decades in the calibration process refer to 1901-1910, 1911-1920, …, and 1991-1999. Because GDP data in some regions were not available before 1950 in the Maddison Project Database 2023 (Bolt and Van Zanden, 2024), we reconstructed the regional GDP in the earlier periods using a linear regression. Specifically, in regions without annual GDP available before 1950, regional annual GDP in the earliest accessible 5 years were fitted against years using a linear regression. This regression was further applied to reconstruct the GDP in the earlier years. If the regional annual GDP was predicted to be negative by the linear regression, the regional annual GDP was assumed to be the same as the nearest year (Fig. S25).

In the FireCCI51-GDP data version, the decadal average of regional total BA was derived from the BA-GDP regressions, while the annual anomalies were from the original FireCCI51-based reconstruction. A ratio of monthly BA to annual total BA from the original FireCCI51-based reconstruction was then applied to correct the monthly BA data in the FireCCI51-GDP version. Finally, the regional total monthly BA after calibration by GDP was applied proportionally to each grid cell based on the gridded burned area from the original FireCCI51-based version.

Table S1. Evaluation of the random forest classification models using the 20% testing set from all years' data (2003-2020). The data over the period of 2003-2020 was split into the training set (80%) and the testing set (20%) in each region. AUC represents Area Under receiver operating characteristic Curves ranging in 0-1, and a larger AUC value indicates better model performance. BAF is burned area fraction in each 0.5°×0.5° grid cell.

Region	**Accuracy**	**AUC (regular BAF)**	**AUC (extreme BAF)**
BONA	97.1%	0.936	0.973
TENA	89.8%	0.851	0.917
CEAM	90.3%	0.909	0.958
NHSA	90.6%	0.936	0.987
SHSA	88.1%	0.908	0.976
EURO	95.5%	0.947	0.966
MIDE	97.7%	0.972	0.968
NHAF	90.9%	0.961	0.989
SHAF	87.8%	0.941	0.984
BOAS	95.1%	0.939	0.971
CEAS	93.1%	0.930	0.968
SEAS	93.3%	0.946	0.988
EQAS	92.1%	0.888	0.950
AUST	87.9%	0.885	0.953

Table S2. Significant trends of annual total burned area from this study, FireCCILT11 and Mouillot and Field (2005) at the global scale and in each region. The trends (unit: million km^2 yr^{-2}) in Table S2 are summarized from Fig. 3 and Fig. 6. Similar trends in the overlapped periods from various datasets are marked in bold colors (red and blue for positive and negative trends, respectively).

Regions	**Trend in this study**	**Trend in FireCCILT11**	**Trend in Mouillot and Field (2005)**
Global	-0.009 (1901-1978) **0.020 (1978-2008)** **-0.050 (2008-2020)**	**0.025 (1995-2011)** **-0.113 (2011-2018)**	**0.041 (1972-1997)**
BONA	0.0003 (1901-1929) **-0.0002 (1929-2017)**	**-0.0002 (1996-2018)**	-0.003 (1901-1920) **-0.0004 (1920-1965)** 0.0008 (1965-1999)
TENA	**0.00005 (1901-1990)** -0.0002 (1993-2020)	**0.001 (1982-1991)**	-0.018 (1901-1909) -0.003 (1909-1965) **0.0003 (1965-1999)**
CEAM	0.00005 (1901-1995) 0.0009 (1995-2004) **-0.0002 (2004-2020)**	-0.0025 (1995-2001) **-0.0001 (2001-2018)**	-0.005 (1901-1905) -0.0002 (1905-1952) 0.0007 (1952-1999)
NHSA	**0.003 (1954-1960)** -0.0003 (1960-2020)	-	**0.0002 (1901-1970)** 0.003 (1970-1989) 0.002 (1989-1999)
SHSA	0.001 (1901-1962) -0.021 (1962-1974) **0.004 (1974-2020)**	-0.007 (1982-1992) **0.009 (1995-2004)** -0.003 (2004-2018)	-0.004 (1901-1934) -0.0003 (1934-1973) **0.014 (1973-1999)**
EURO	0.00002 (1901-1978) 0.0002 (1978-1991) -0.0002 (1991-2020)	0.0007 (1995-2012) -0.002 (2012-2018)	-0.00002 (1901-1971) 0.0005 (1971-1980) -0.0001 (1980-1999)
MIDE	0.00001 (1901-1985) 0.0003 (1985-1994) **0.00001 (1994-2020)**	**0.0006 (1995-2017)**	-0.00003 (1901-1999)
NHAF	**0.005 (1901-1922)** -0.008 (1922-1957) **-0.004 (1957-2020)**	**-0.019 (2007-2018)**	**0.004 (1901-1977)** 0.014 (1977-1999)
SHAF	-0.004 (1901-1979) **0.011 (1979-2011)** **-0.019 (2011-2020)**	**0.022 (1995-2012)** **-0.087 (2012-2018)**	-
BOAS	-0.0006 (1901-1941) 0.0009 (1941-1997) -0.0009 (1997-2020)	-	0.021 (1901-1915) -0.0001 (1915-1999)
CEAS	**0.0024 (1956-2006)** **-0.005 (2006-2020)**	**0.016 (1995-2002)** **-0.007 (2002-2018)**	-0.002 (1953-1981) **0.009 (1981-1999)**
SEAS	**-0.0002 (1901-1994)** **0.0014 (1994-2020)**	0.001 (1985-1993) **0.001 (1998-2018)**	**-0.004 (1901-1916)** 0.002 (1916-1968) **0.005 (1968-1999)**

EQAS	-	-	0.0002 (1901-1964) 0.002 (1964-1999)
AUST	**-0.0026 (1979-2020)**	-	**-0.006 (1936-1999)**

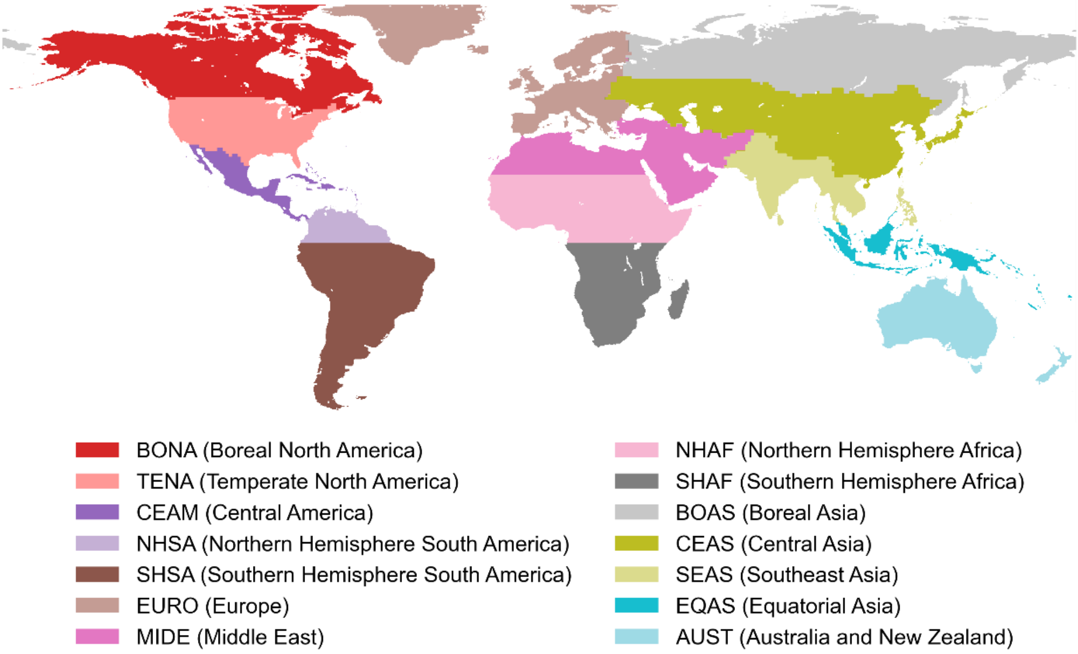

Figure S1. Map of GFED regions used in this study following Van Der Werf et al. (2017).

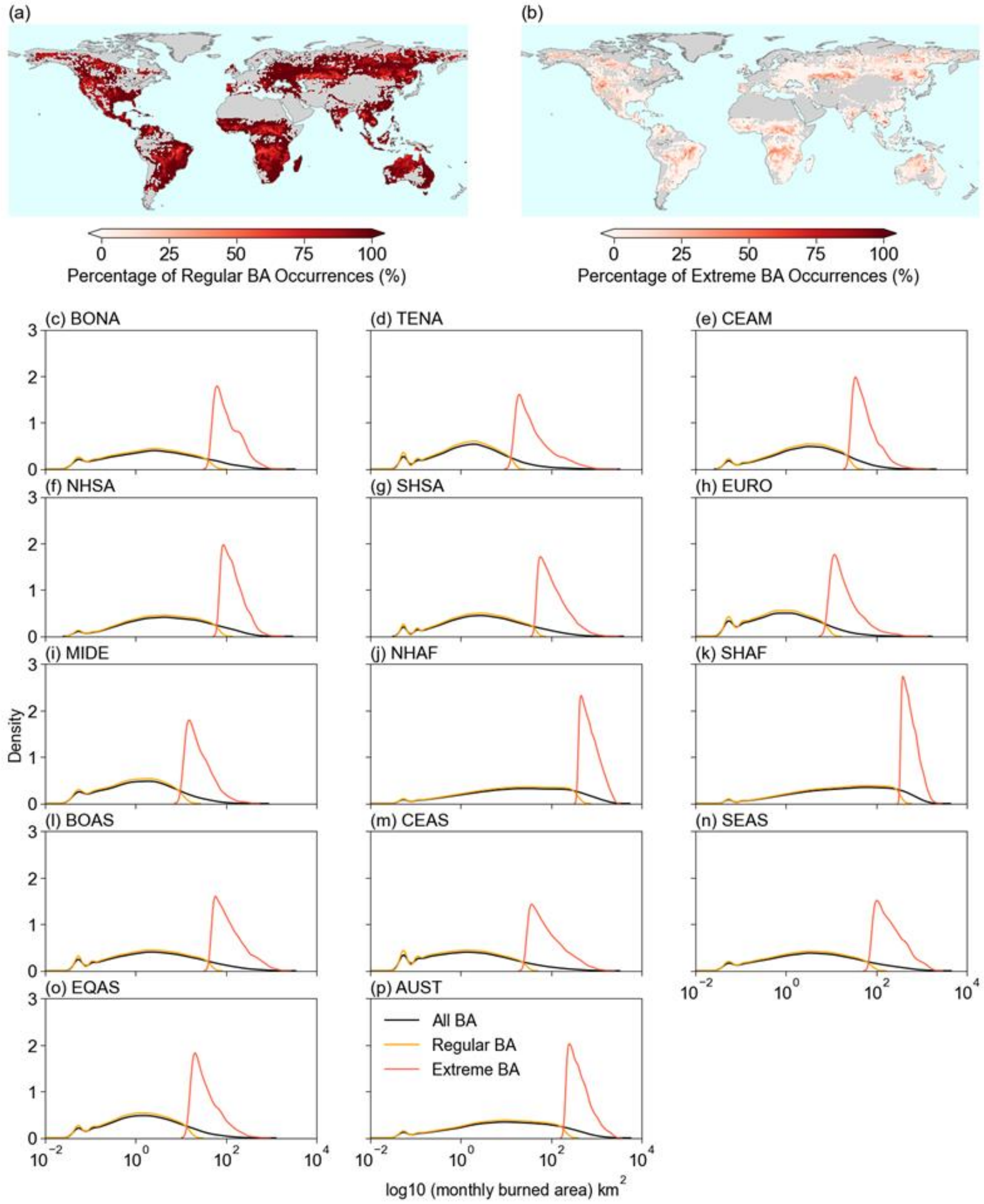

Figure S2. Distribution of regular and extreme monthly burned area within half-degree grid cells based on FireCCI51 in 2003-2020. (a-b) Spatial distribution of fire occurrence (%) (i.e., the number of months with fire occurrence divided by the total month number in 2003-2020 multiplying 100%) for the regular and extreme burned area. (c-p) Kernel density distribution of monthly burned area within half-degree grid cells in 2003-2020 for all (black lines), regular (orange lines) and extreme (red lines) burned area in various regions.

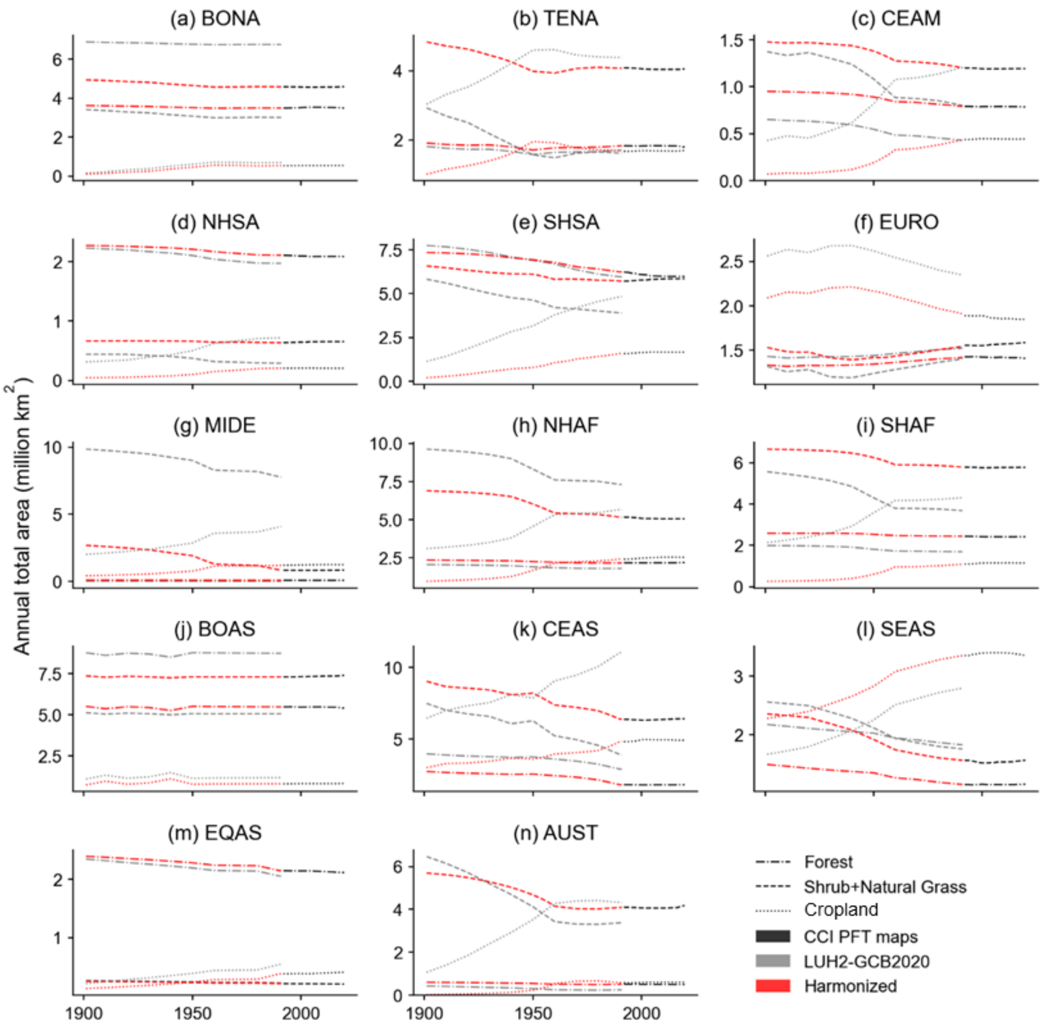

Figure S3. Time series of annual total area of different land use types using the CCI land cover maps (black), LUH2-GCB2020 (grey) and the harmonized data (red) in each region.

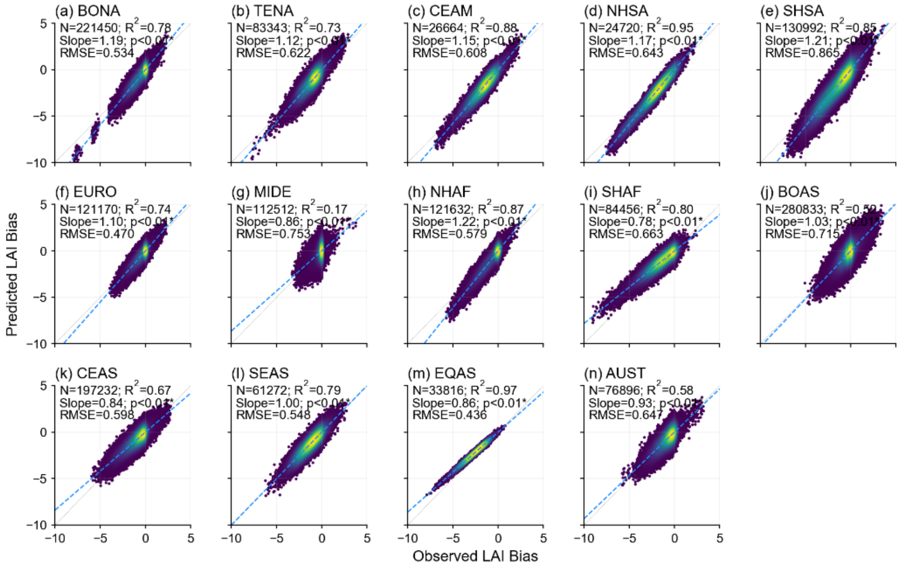

Figure S4. Evaluation of the LSTM regressions for predicting the LAI biases between GIMMS LAI4g and TRENDY v11 using the testing set (20%) of all years' data (1982-2020) in each region.

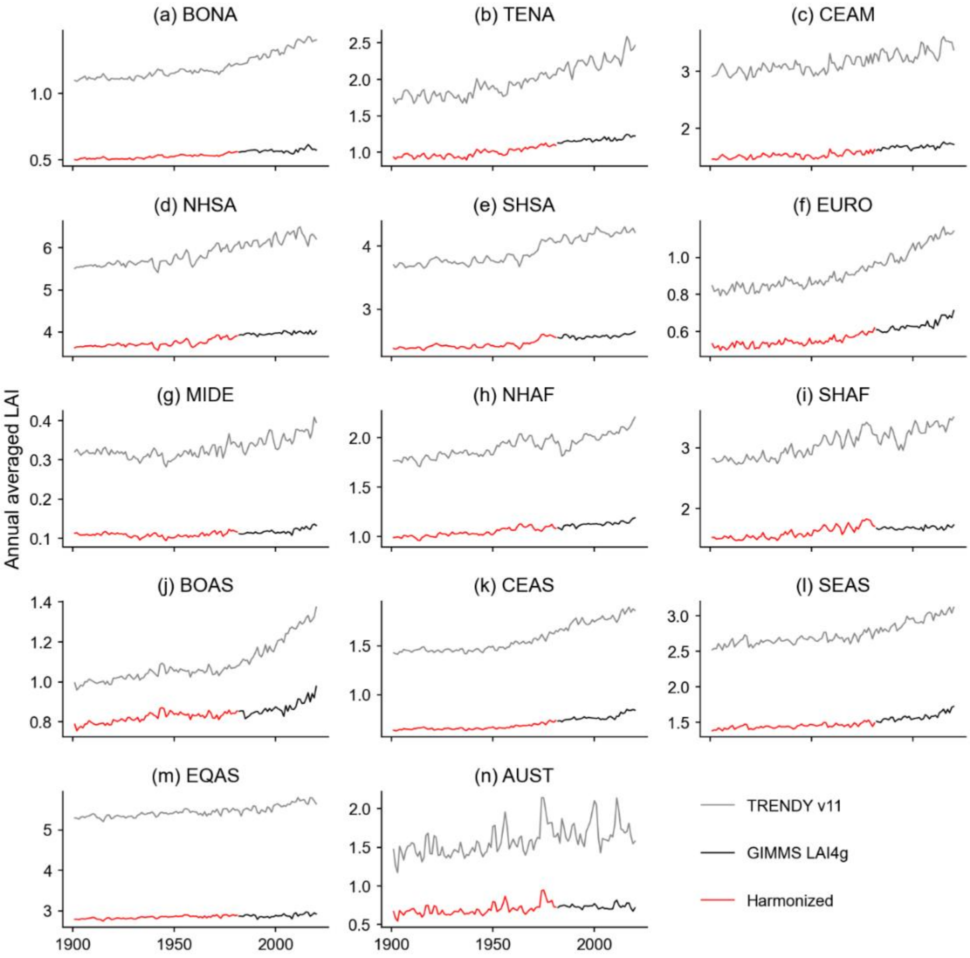

Figure S5. Time series of annual regional average LAI from GIMMS LAI4g (black), TRENDY v11 (grey) and the harmonized data (red) in each region.

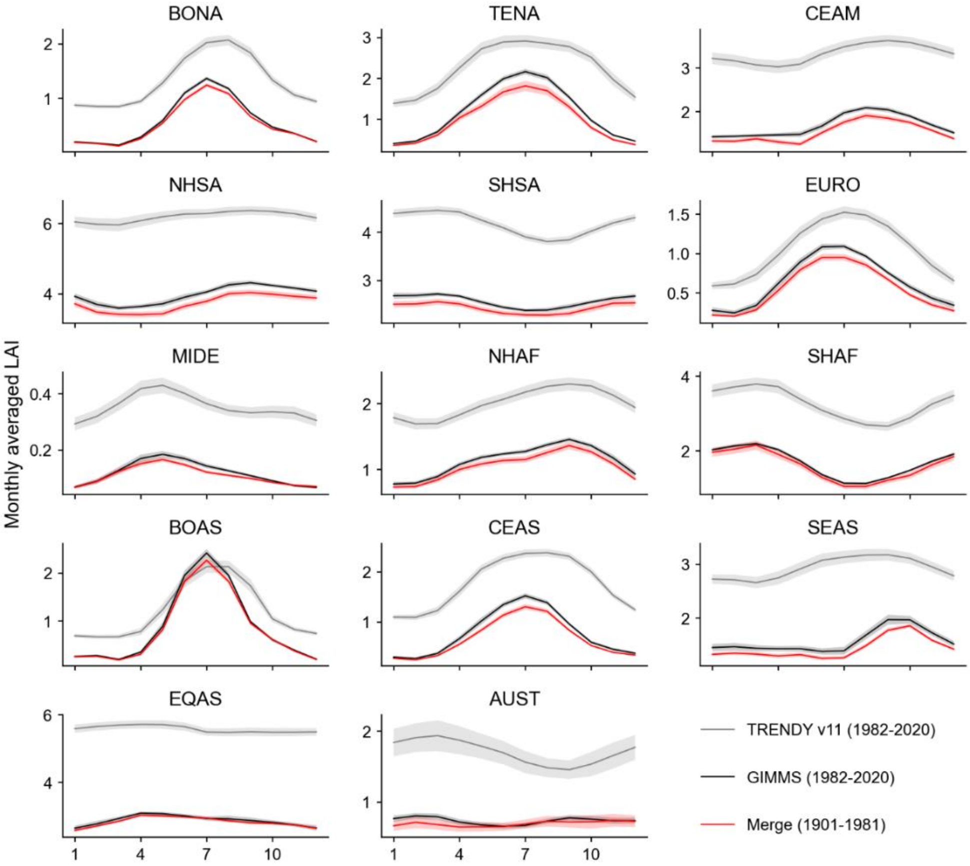

Figure S6. Seasonality of regional average LAI from GIMMS LAI4g (black), TRENDY v11 (grey) and the harmonized data (red) in each region.

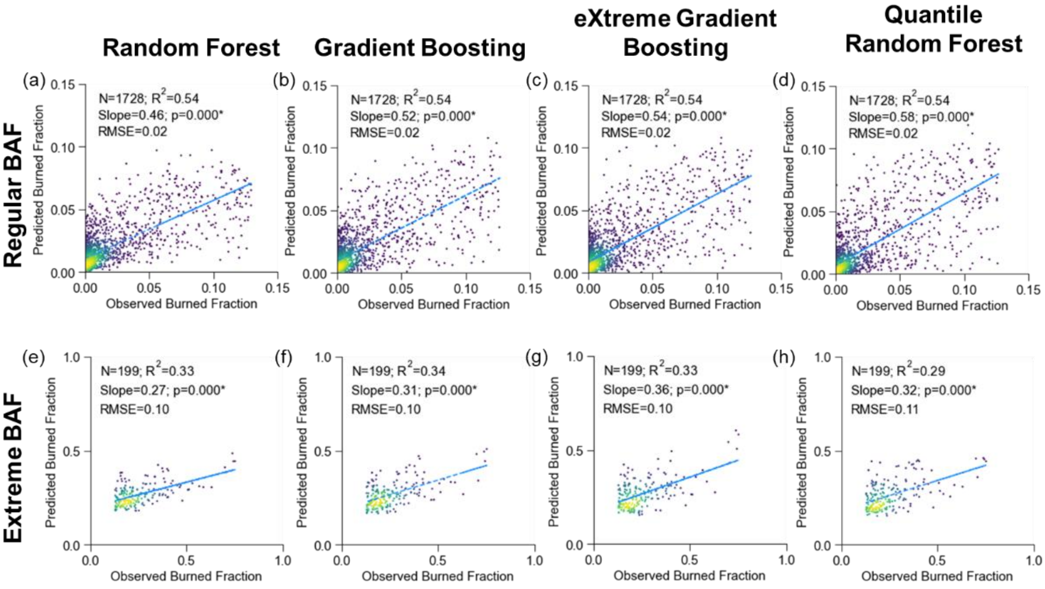

Figure S7. Evaluation of different machine learning regression models for regular (a-d) and extreme BAF (e-h), respectively using the testing set (20%) of 2010 in NHAF.

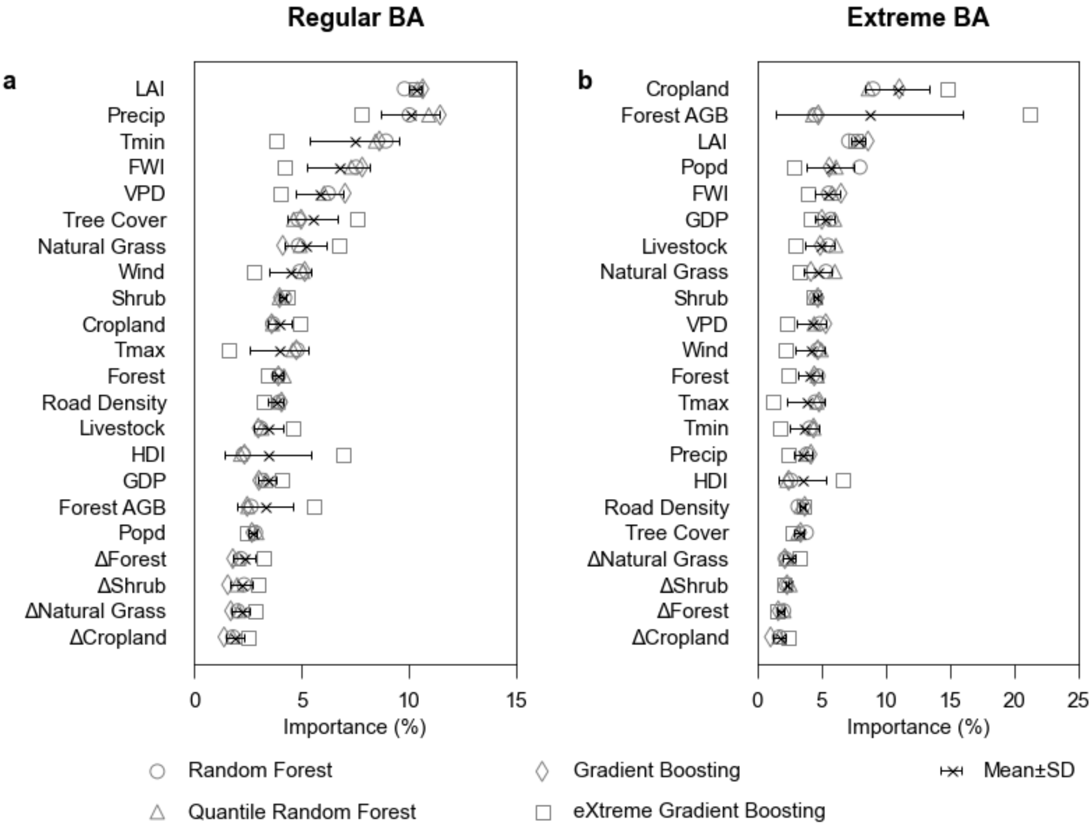

Figure S8. Feature importance for regular (a) and extreme BAF (b), respectively, in NHAF using different machine learning regression models.

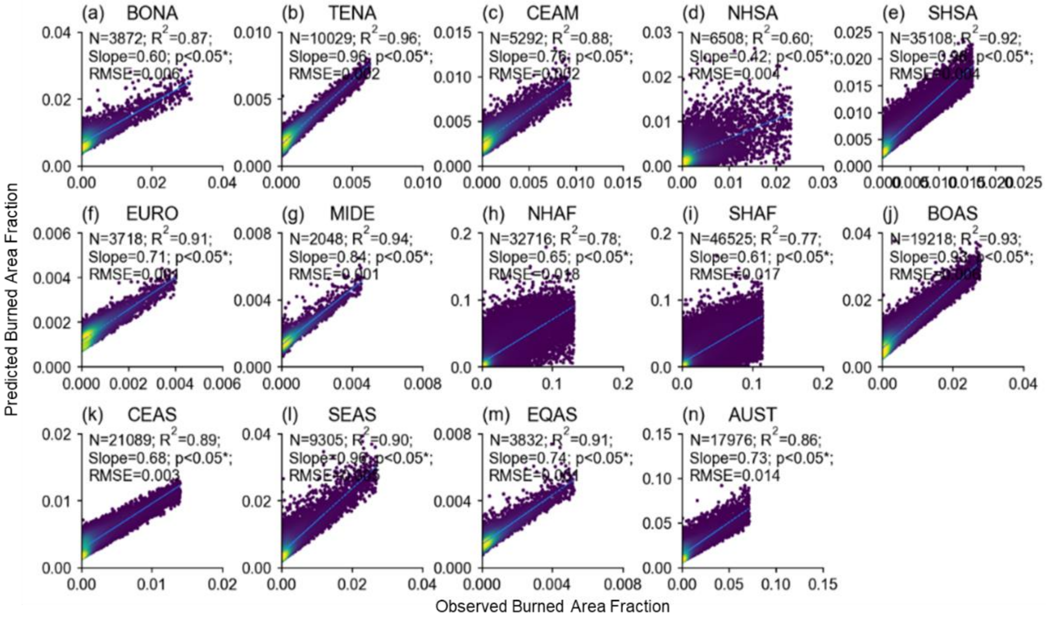

Figure S9. Evaluation of the LSTM regression models for the regular BAF using the testing set (20%) of all years' data (2003-2020) in each region.

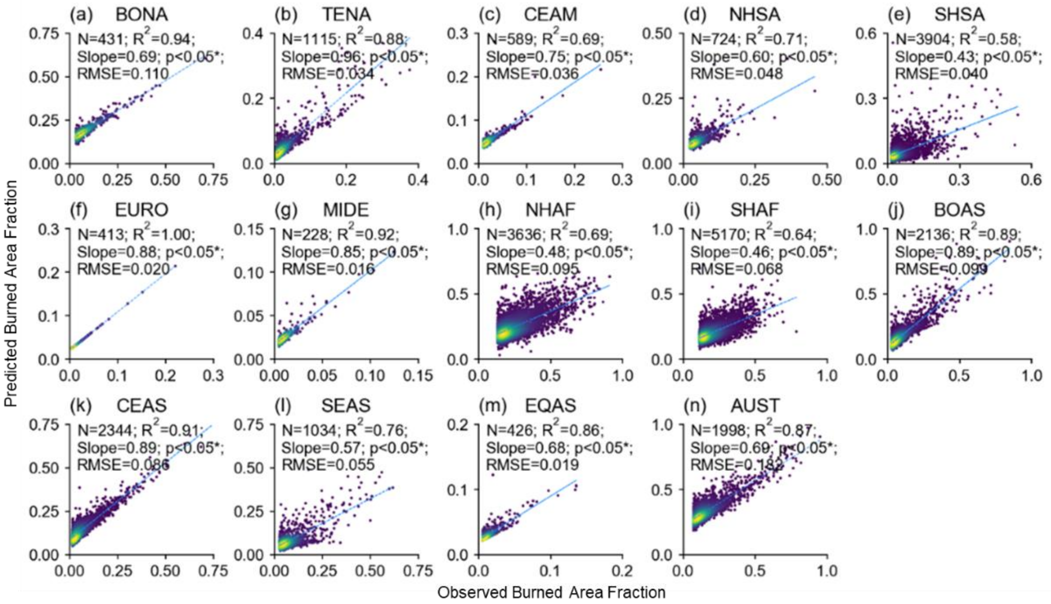

Figure S10. Same as Figure S9 but for extreme BAF.

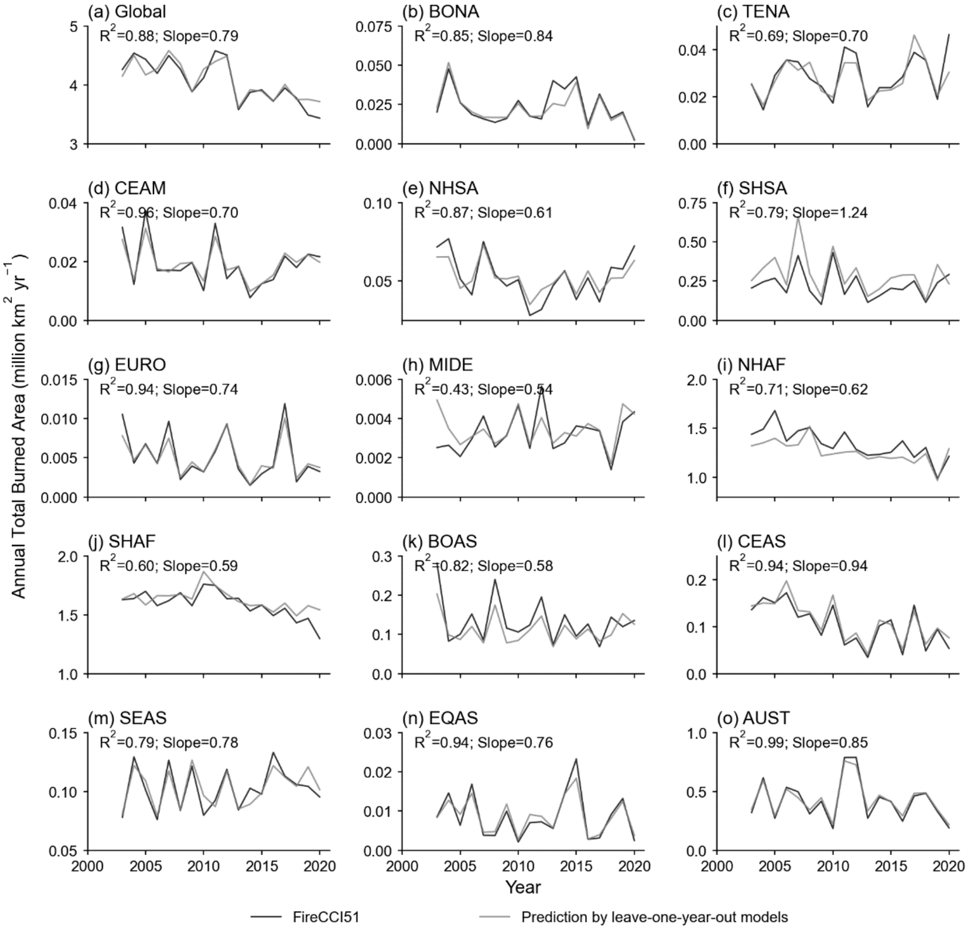

Figure S11. Time series of annual total burned area across the globe (a) and in each region (b~o) from FireCCI51 (black lines), and from predictions by the leave-one-year-out methods (grey lines). R^2 and slopes from the linear regressions between the two time series are also shown.

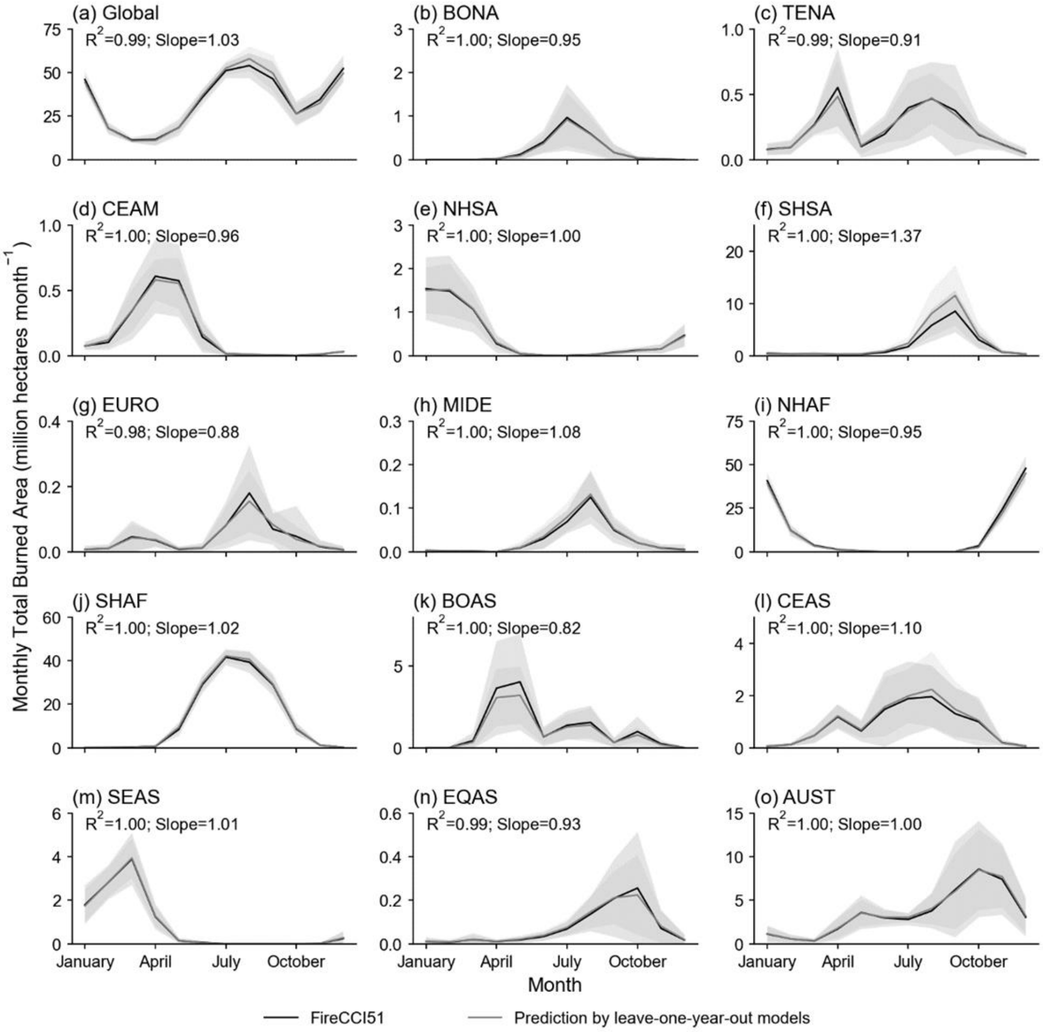

Figure S12. Seasonality of the total burned area at the global scale (a) and in each region (b-o) from FireCCI51 (2003-2020) and predictions by the leave-one-year-out methods (2003-2020). Lines and shaded area represent the average and standard deviation of monthly values across multiple years, respectively. R^2 and slopes from the linear regressions between the two time series are also shown.

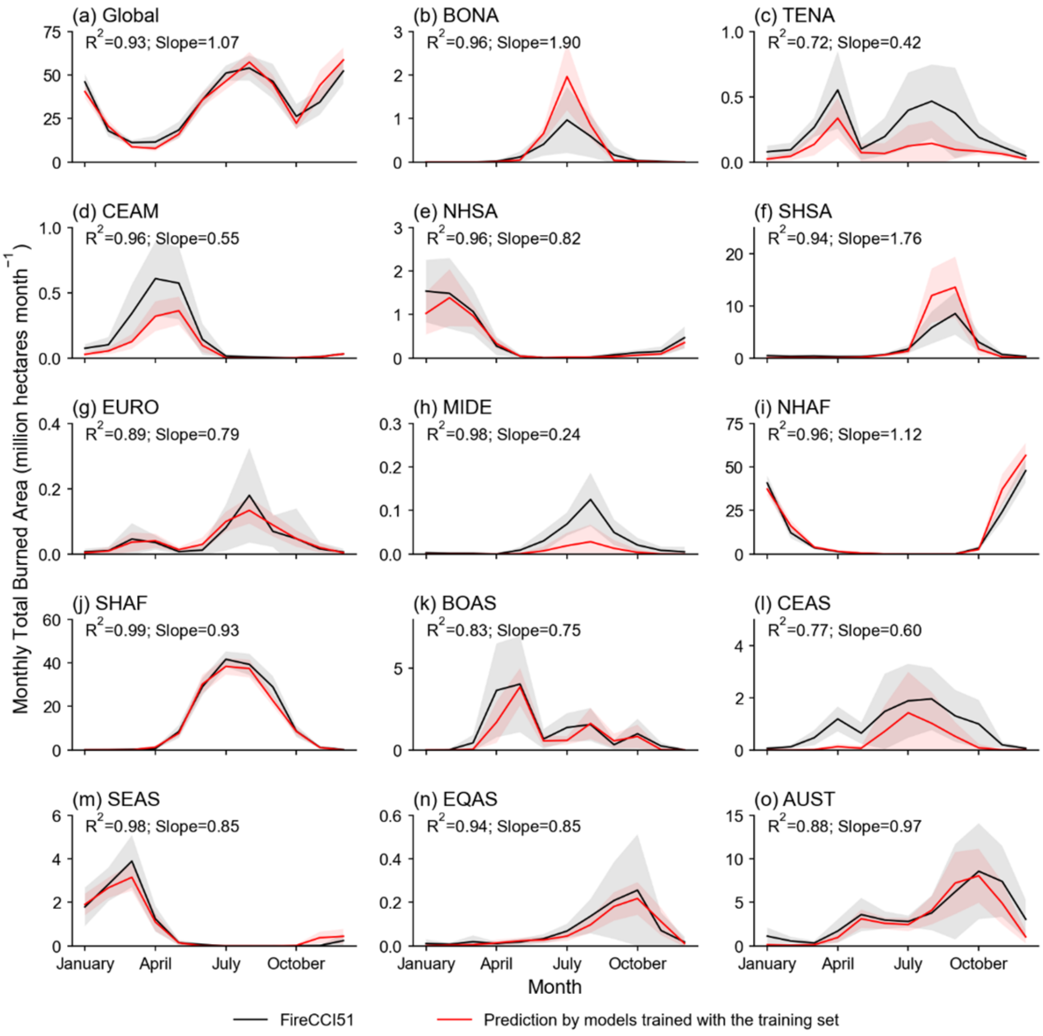

Figure S13. Same as Figure S12 but using predictions (1901-2020) by models trained with the training set (80% of all years' data during 2003-2020) instead. For the seasonality of the burned area, there are two peaks centered in August and December at the global scale (Fig. S13a). The December centered peak is mainly contributed NHAF (Fig. S13i), while the August peak mainly by SHSA and SHAF (Fig. S13f, S13j). Moreover, the monthly total burned area in 1901-2020 (red lines) are obviously lower than 2003-2020 (black lines) in TENA, CEAM, MIDE and CEAS (Fig. S13c, S13d, S13h, S13l), but apparently higher than 2003-2020 (black and grey lines) in BONA and SHSA (Fig. S13b, S13f).

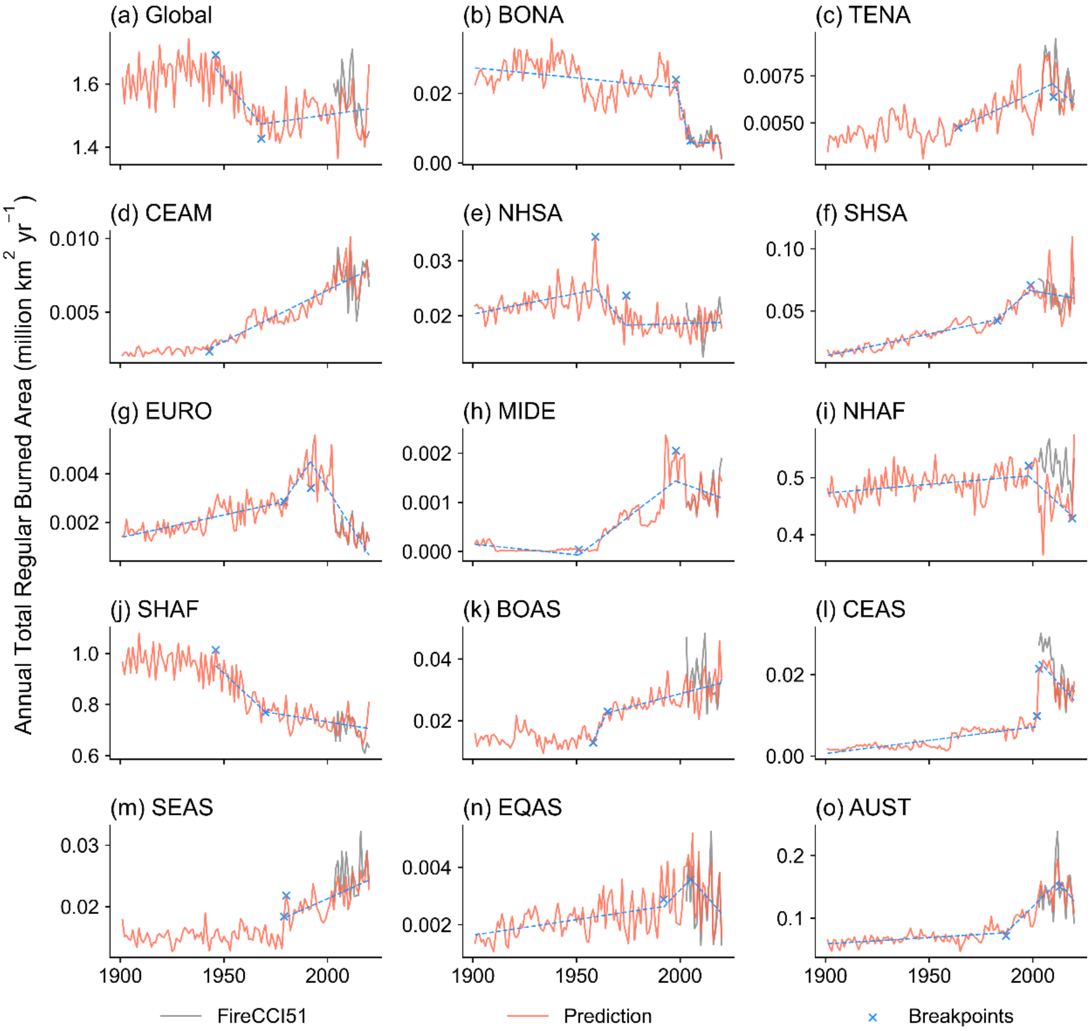

Figure S14. Time series of annual total burned area for regular fires across the globe (a) and in each region (b~o) from FireCCI51 (black lines, 2003~2020) and predictions (red lines, 1901~2020). The breakpoints and significant slopes (p-value < 0.05) in blue were also shown (Section 2.2 in the main text).

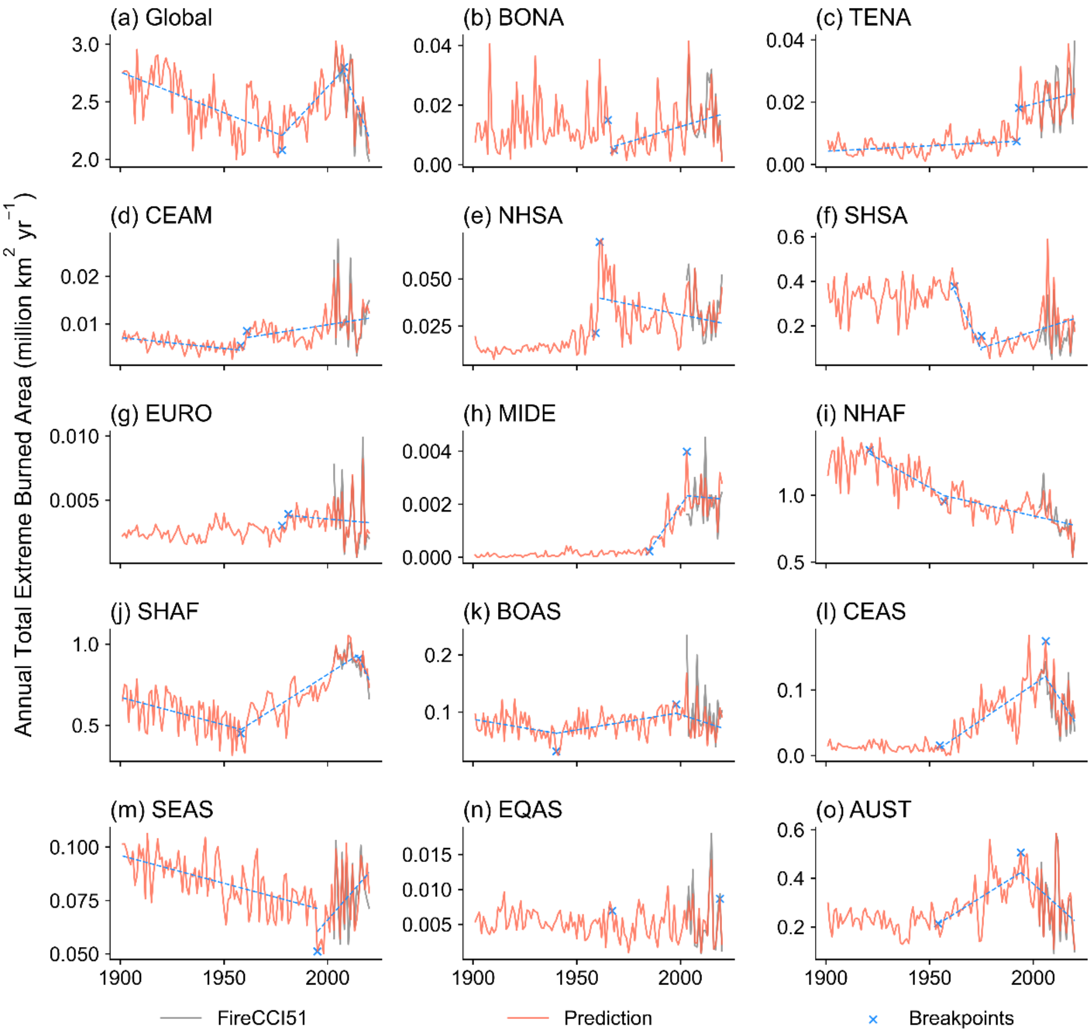

Figure S15. Same as Figure S14 but for extreme fires.

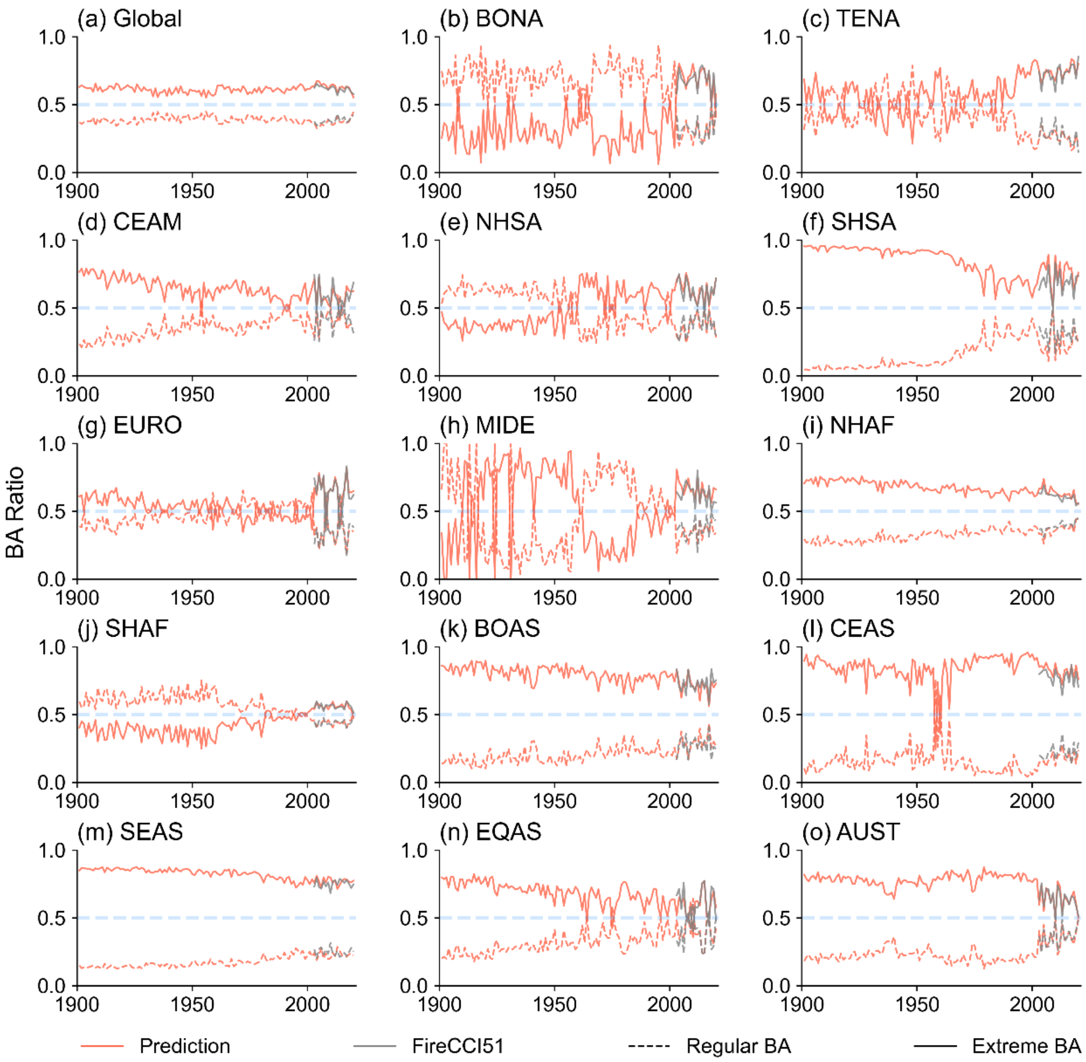

Figure S16. Time series of annual burned area ratios across the globe (a) and in each region (b~o) for regular (dotted lines) and extreme (solid lines) burned area from FireCCI51 (grey lines, 2003~2020) and predictions (red lines, 1901~2020). Burned area ratios of a certain fire type is calculated by the annual burned area of this fire type divided by the annual total burned area.

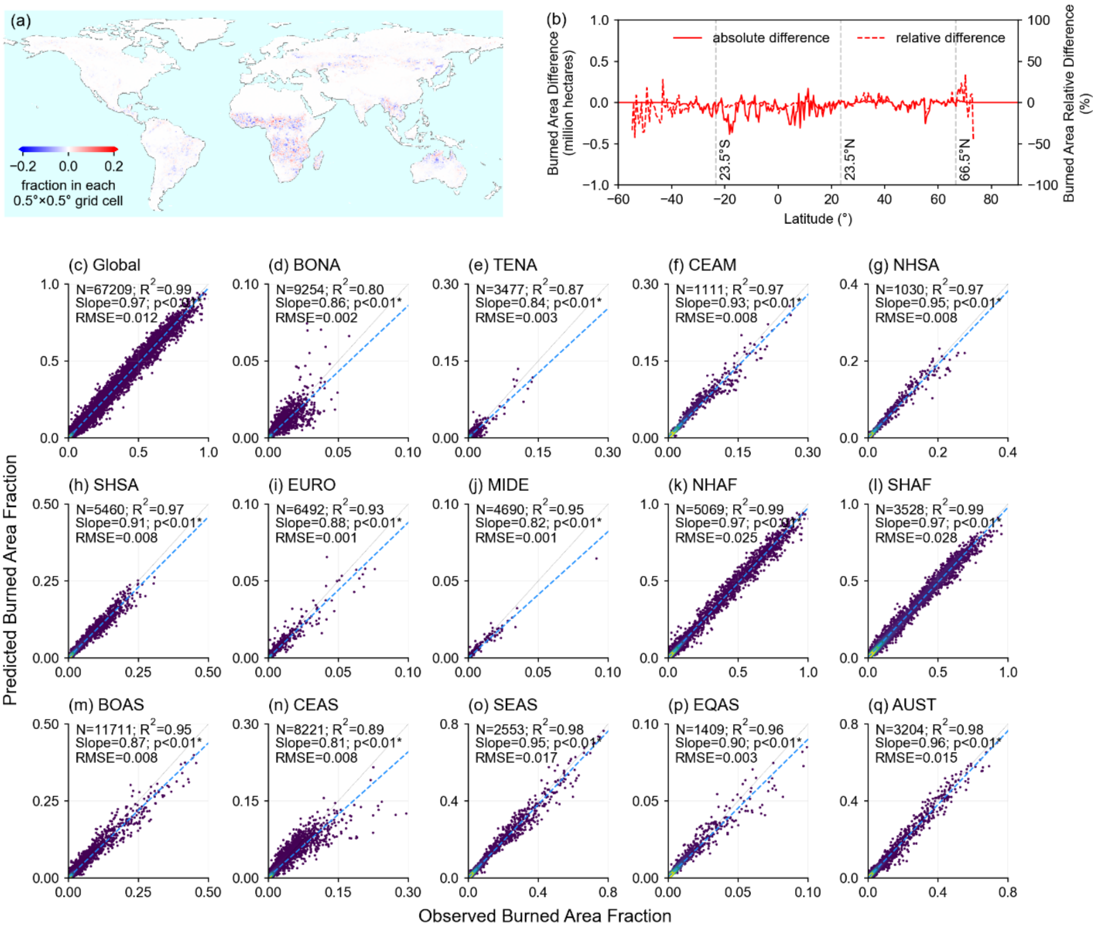

Figure S17. Validation of the multi-year (2003~2020) average burned area predicted from GFED5 against the GFED5 burned area using the leave-one-year-out method. (a) Map of burned area difference between predictions and GFED5 (the former minus the latter). (b) Longitudinal sum of burned area difference using the area fraction difference map from (a) multiplied by the land area in each 0.5°×0.5° grid cell, where solid and dotted lines represent absolute and relative difference from the GFED5 observations. (c-q) Scatter plots of burned area fraction for each region from GFED5 and our predictions. RMSE represents rooted mean squared error between observations and predictions.

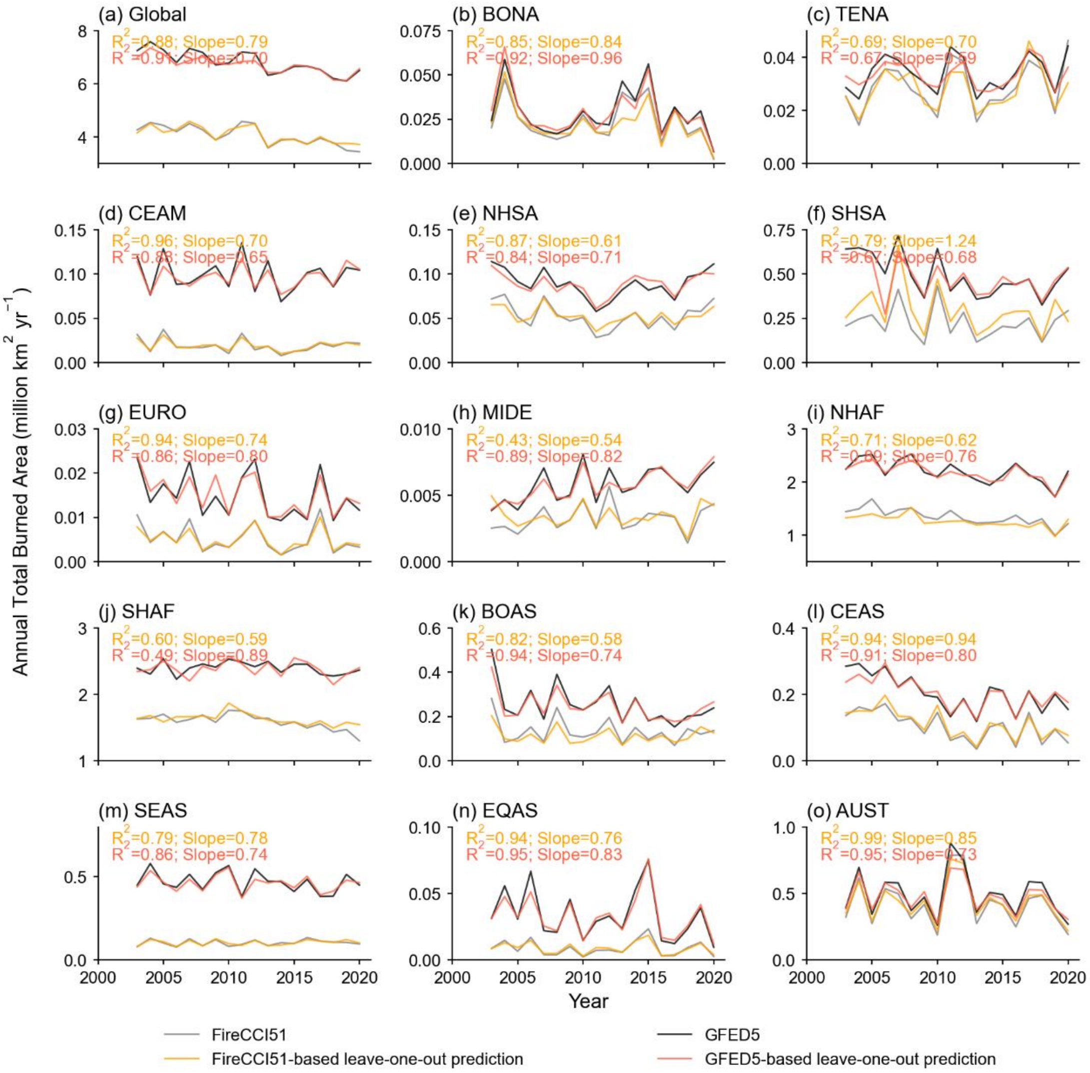

Figure S18. Time series of annual total burned area across the globe (a) and in each region (b~o) from FireCCI51 (grey lines) and GFED5 (black lines) observations, and from predictions by the leave-one-year-out methods based on FireCCI51 (orange lines) and GFED5 (red lines). R^2 and slopes from the linear regressions between observation and corresponding prediction are also shown.

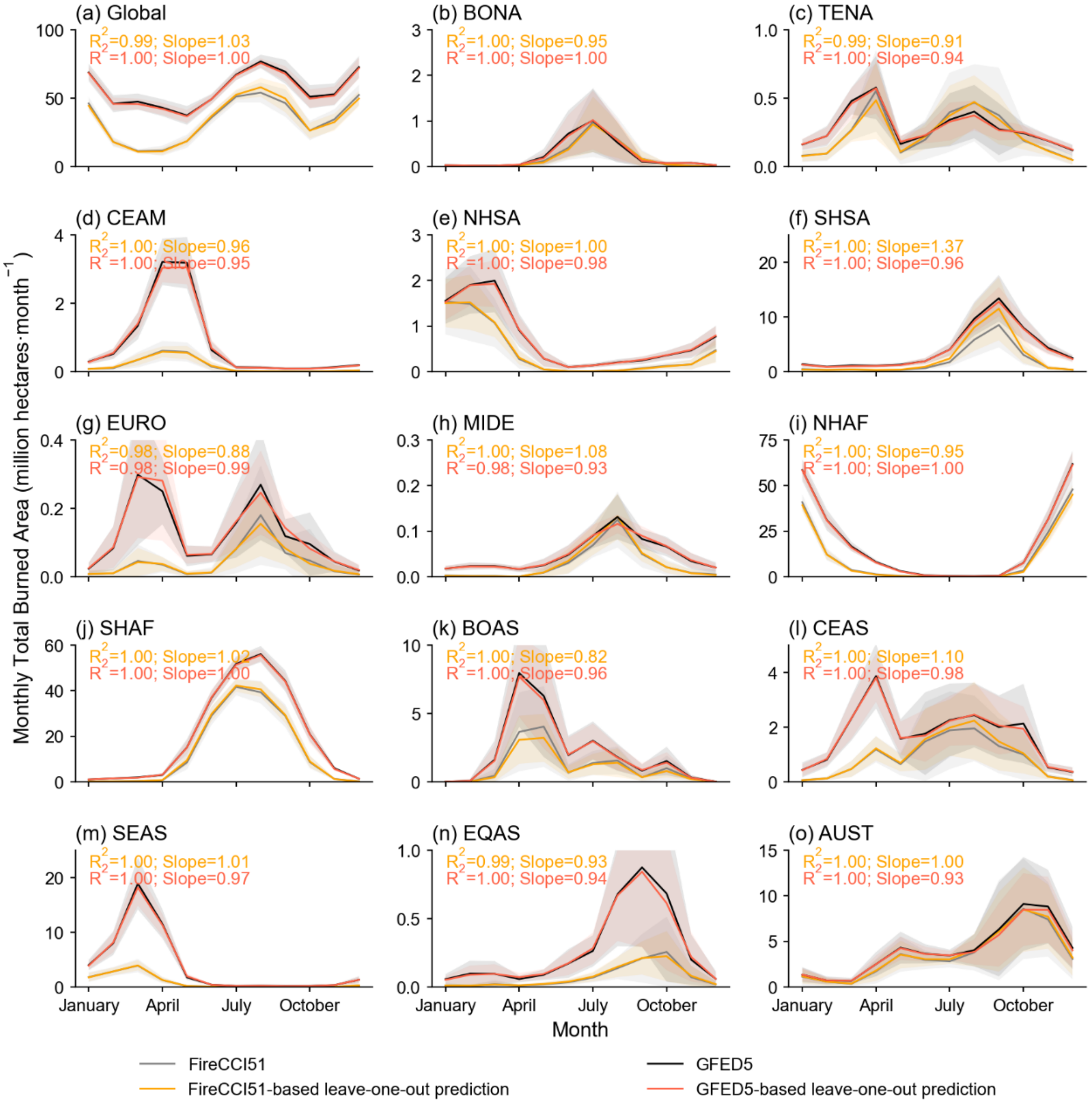

Figure S19. Seasonality of the total burned area (2003-2020) at the global scale (a) and in each region (b-o) from FireCCI51 (grey lines) and GFED5 (black lines), and predictions by the leave-one-year-out methods based on FireCCI51 (orange lines) and GFED5 (red lines). Lines and shaded area represent the average and standard deviation of monthly values across multiple years, respectively. R^2 and slopes from the linear regressions between observations and predictions are also shown.

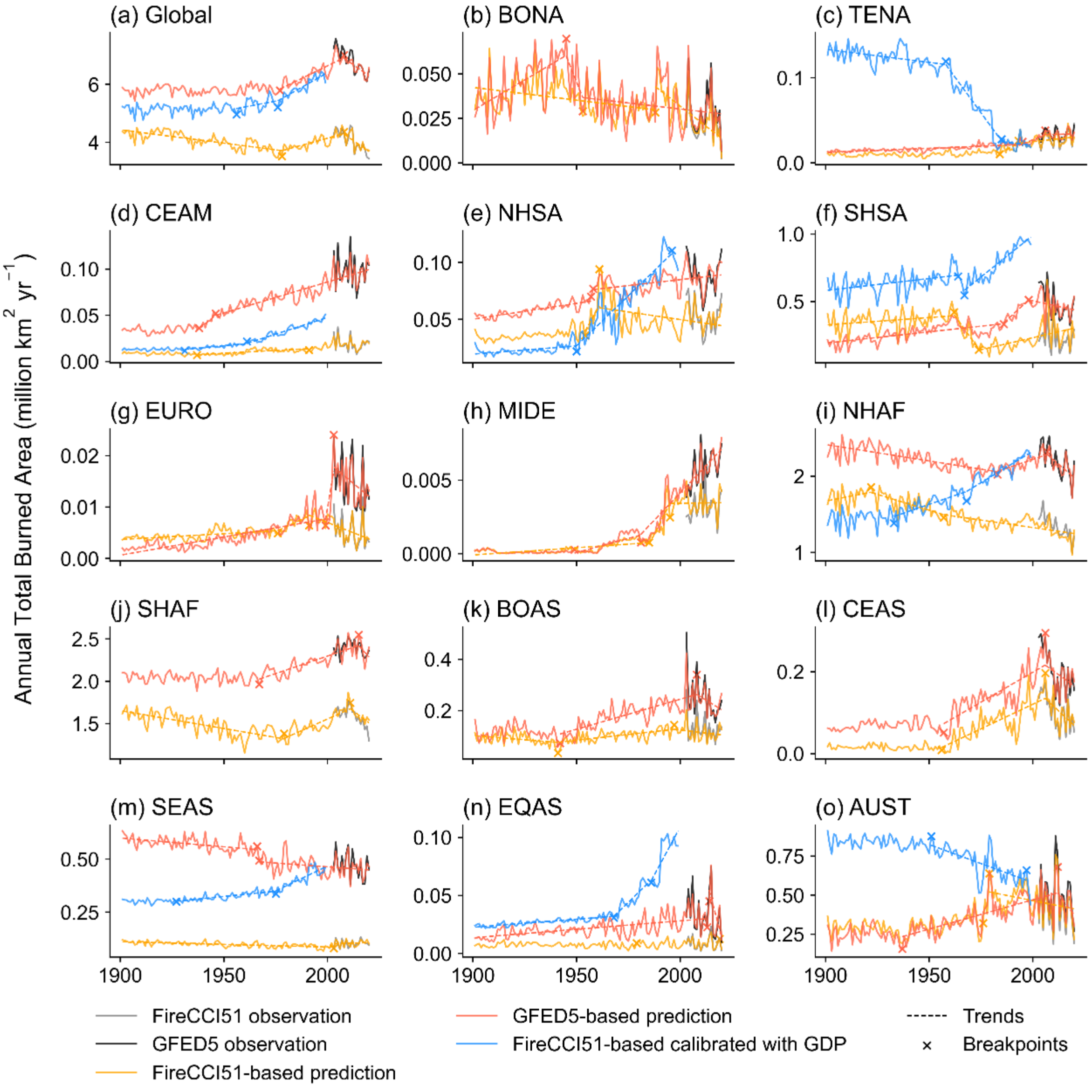

Figure S20. Time series of annual total burned area across the globe (a) and in each region (b~o) from FireCCI51 (grey lines, 2003~2020) and GFED5 (black lines, 2003~2020), and predictions based on FireCCI51 (orange lines, 1901~2020), GFED5 (red lines, 1901~2020) and calibrated with GDP before 2000 (blue lines, 1901-1999). The breakpoints and significant trends (dotted lines, p-value < 0.05) are also shown (Section 2.2 in the main text).

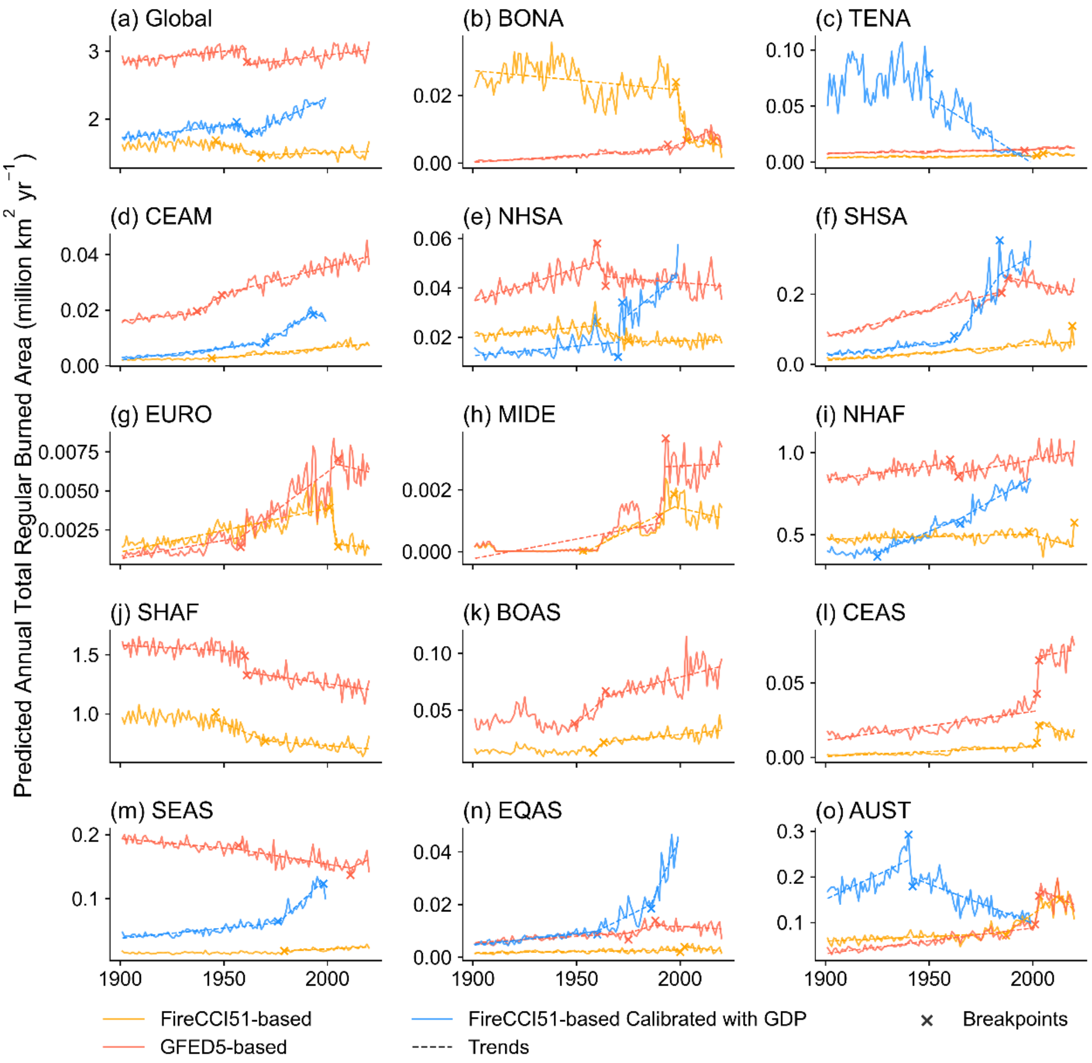

Figure S21. Time series of predicted annual total regular burned area across the globe (a) and in each region (b~o) from the original FireCCI51-based (orange lines, 1901~2020), GFED5-based (red lines, 1901~2020) and the FireCCI51-GDP (blue lines, 1901-1999) product versions. The breakpoints and significant trends (dotted lines, p-value < 0.05) are also shown (Section 2.2 in the main text).

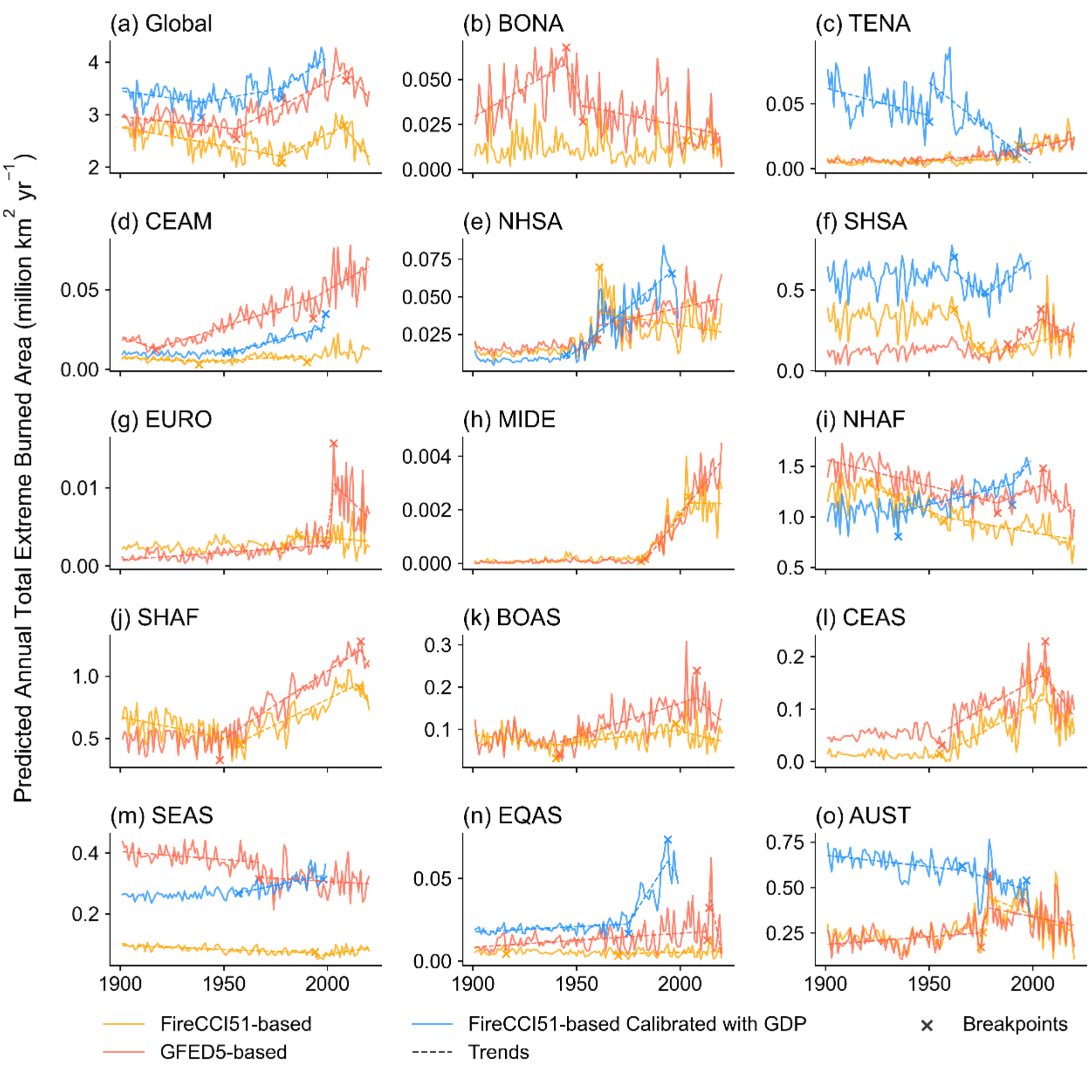

Figure S22. Same as Figure S21 but for extreme burned area.

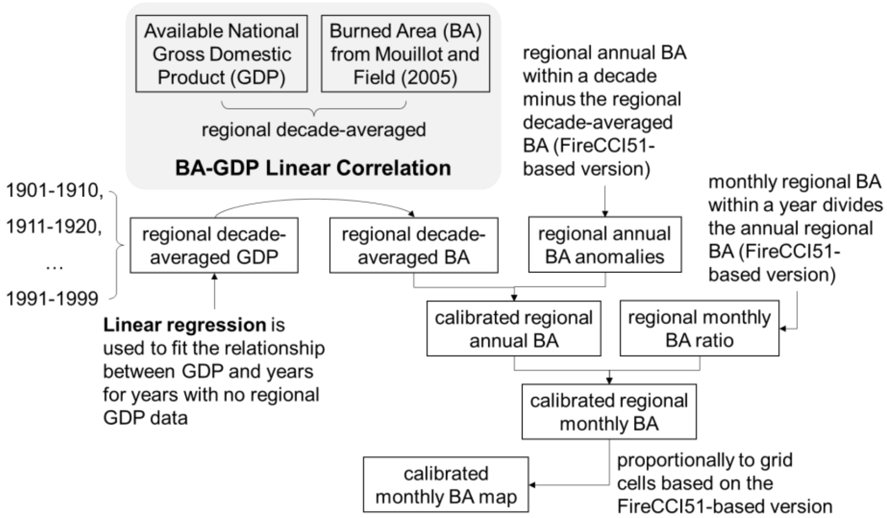

Figure S23. Workflow of calibrating the FireCCI51-based reconstruction burned area with GDP from the Maddison Project Database 2023 (Bolt and Van Zanden, 2024) and burned area from Mouillot and Field (2005) at the regional scale before 2000.

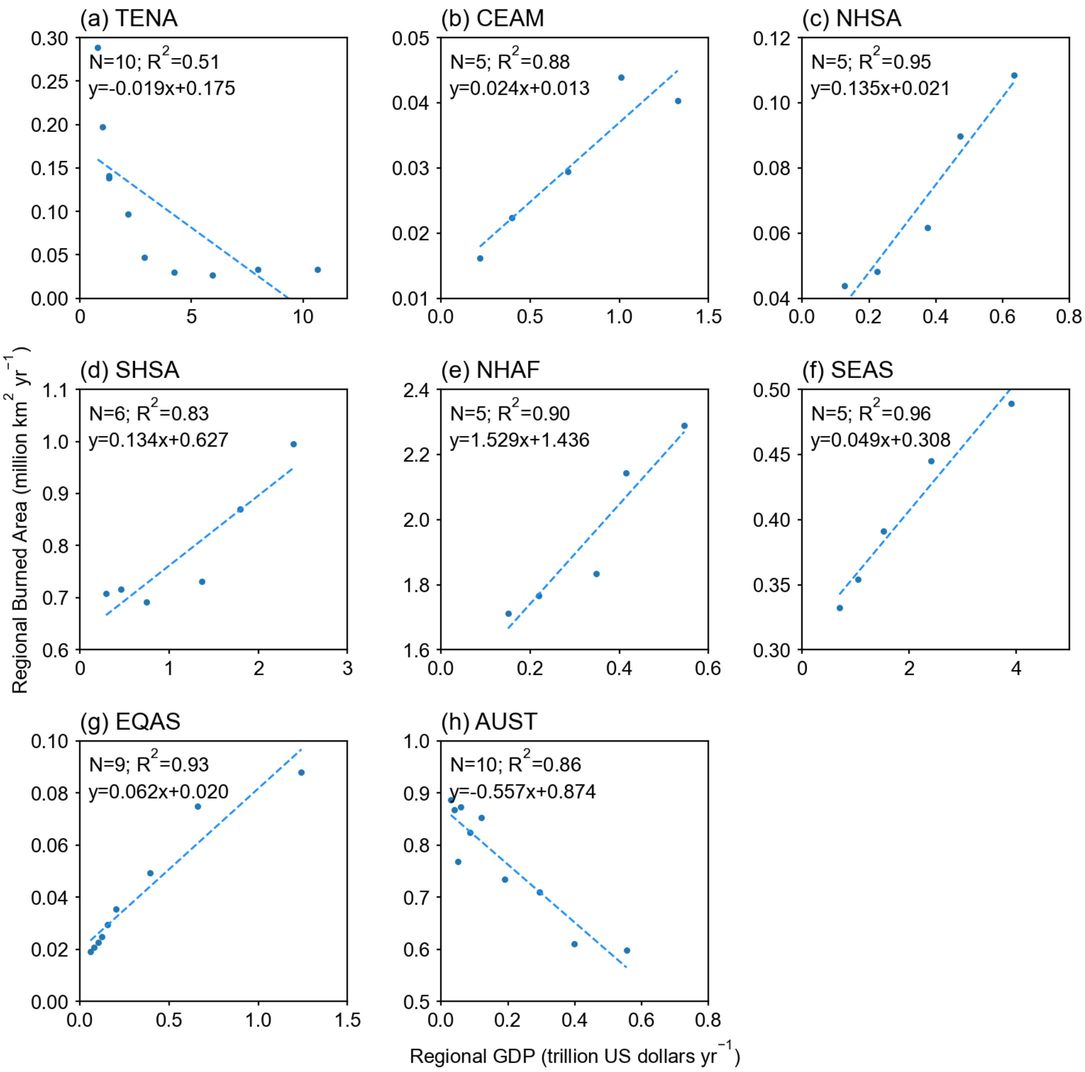

Figure S24. Correlations between the regional total decadal burned area from Mouillot and Field (2005) and GDP from the Maddison Project Database 2023 (Bolt and Van Zanden, 2024) in each region. Solid lines indicate the significant (p-value < 0.05) linear correlations, and dashed lines for non-significant.

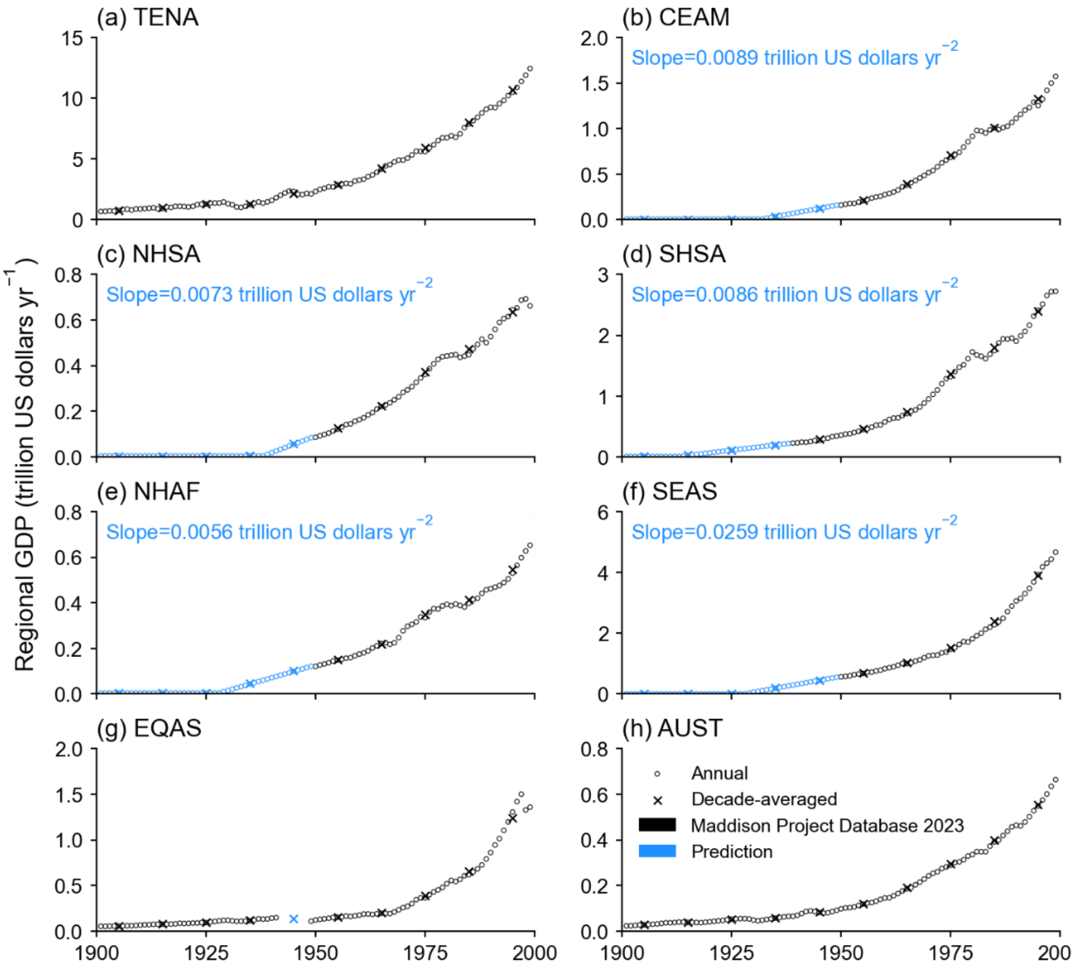

Figure S25. Time series of regional annual (circles) and decade-averaged (crosses) GDP from the Maddison Project Database 2023 (black) (Bolt and Van Zanden, 2024) and our reconstructed GDP (blue, see details below). Only regions with significant correlations (p-value < 0.05) in Figure S24 are shown here. In regions without annual GDP available before 1950, regional annual GDP in the earliest accessible 5 years were fitted against years using a linear regression. This regression was further applied to reconstruct the GDP in the earlier years. If the regional annual GDP was predicted to be negative by the linear regression, the regional annual GDP was assumed to be the same as the nearest year.

References

Bolt, J. and van Zanden, J. L.: Maddison-style estimates of the evolution of the world economy: A new 2023 update, Journal of Economic Surveys, n/a, https://doi.org/10.1111/joes.12618, 2024.

Mouillot, F. and Field, C. B.: Fire history and the global carbon budget: a 1°× 1° fire history reconstruction for the 20th century, Global Change Biology, 11, 398-420, https://doi.org/10.1111/j.1365-2486.2005.00920.x, 2005.

van der Werf, G. R., Randerson, J. T., Giglio, L., van Leeuwen, T. T., Chen, Y., Rogers, B. M., Mu, M., van Marle, M. J. E., Morton, D. C., Collatz, G. J., Yokelson, R. J., and Kasibhatla, P. S.: Global fire emissions estimates during 1997–2016, Earth Syst. Sci. Data, 9, 697-720, 10.5194/essd-9-697-2017, 2017.